A Study of Case II Transport by Laser Interferometry

C. J. Durning,* M. M. Hassan, H. M. Tong,[†] and K. W. Lee[‡]

Department of Chemical Engineering, Materials Science and Mining, Columbia University, New York, New York 10027, IBM Corporation, East Fishkill, New York 12533, and IBM Corporation, T. J. Watson Research Center, Yorktown Heights, New York 10598

Received October 25, 1994; Revised Manuscript Received March 6, 1995[®]

ABSTRACT: Laser interferometry is found to be a very convenient technique for studying gradient diffusion in the poly(methyl methacrylate)/methanol (PMMA/MeOH) system. We studied the process in initially dry, supported PMMA films suddenly immersed in liquid MeOH and examined the effects of temperature and sample thermal history. Over the range of conditions studied, the diffusion process was entirely Case II. A simple model was developed to predict the time dependence of the intensity of light reflected from a supported film during Case II. An FFT algorithm made it possible to accurately match the reflected intensity data and the model predictions to determine the key parameters defining the Case II process: The volume fraction of methanol behind the Case II front (ϕ_e), the front velocity (v), and the front reflectivity (rf_2). Free-volume theory describes the temperature dependence of v very well and enables calculation of the individual apparent activation energies for methanol diffusion in and viscous flow of the dry glassy polymer. The polymer sample's thermal history has a large effect on v: Samples quenched through T_{g2} faster show higher v with a lower apparent activation energy; free-volume theory can describe this thermal history effect fairly well. Over the whole range of conditions examined, we observed rf_2 at least an order of magnitude smaller than that calculated from the Fresnel formula for a true discontinuity in fluid concentration, proving that the sharp Case II front has a finite width on the order of 100 nm. However, the current theory for Case II cannot fully explain the trends found in rf_2 with temperature or with the sample's thermal history.

Introduction

Case II transport is an unusual form of gradient diffusion found in glassy polymer/simple fluid systems. Concentration profiles during Case II show wavelike self-similarity, $C = f(\mathbf{r}-\mathbf{v}t)$, unlike those during ordinary "Fickian" diffusion which show the self-similarity implied by the diffusion equation, $C = f(\mathbf{r}/(\alpha t)^{1/2})$ (here $\mathbf{r}$ is position, t is time, and v and α are constants). Case II appears often in applications, and there is no widely accepted predictive model at present. A better, first-principles understanding is, therefore, an important goal.

A phenomenological understanding of Case II has been developed through careful, macroscopic sorption experiments (e.g., refs 1–4). However, there remains a need for further systematic investigation to establish clearly the effects of driving force, polymer thermal history, polymer molecular weight, polymer chain branching, cross-linking, and the nature of the fluid. Some progress has been made toward this by Kramer et al.[5–10] using Rutherford backscattering (RBS) to examine the effects of driving force and the nature of the fluid.

In what follows we describe the application of laser interferometry to the systematic study of Case II. First, we summarize the current understanding of the process and then summarize the interferometric method where a simple optical model for the steady-periodic interferometric signal during Case II is presented. Finally, experimental data exploring the effects of temperature and thermal history on the Case II transport of methanol in poly(methyl methacrylate) are presented and analyzed.

Case II Transport

Phenomenology. Case II is a non-Fickian or "viscoelastic" gradient diffusion phenomenon in polymer/fluid systems. It is an extreme deviation from Fickian diffusion when *nonlinearities dominate*.[11] It is observed in glassy polymer/fluid systems when the change in composition accompanying interdiffusion is large enough so that the local diffusion Deborah number decreases several orders, probably through $O(1)$. [The diffusion Deborah number[12,13] gives the ratio of the dominant material relaxation time of the mixture to the time scale for interdiffusion.]

Case II is usually studied by a one-dimensional integral sorption experiment: A dry, glassy film of depth l is suddenly exposed to fluid at unity activity. The fluid sorbs into the film to ultimately establish a homogeneous equilibrium state. The RBS experiments by Kramer et al.[5–10] showed exactly how the concentration profiles develop during Case II (Figure 1). Initially there is an "induction" period where the fluid concentration at the film surface increases very slowly toward the equilibrium value; a nascent concentration profile is established near the film surface (Figure 1a). At a certain critical value (C_C), the surface concentration abruptly increases toward the equilibrium value (C_e), creating a sharp concentration front (Figure 1b). The front, with a fluid "precursor" then propagates into the film at a constant speed (Figure 1c). The RBS experiments show that the steady-state profile can be represented empirically as a step-exponential function, as first proposed by Peterlin in 1965.[14]

Theory. A theory for one-dimensional viscoelastic diffusion was developed by Durning and Tabor in 1986.[15] Fu and Durning[11] showed that it reduces to Thomas and Windle's (TW) model[16] in a retarded motion limit, appropriate for the Case II process. The TW model is the simplest one for Case II based on first principles.[11] Hui et al.[78] analyzed the TW model for the steady-state fluid concentration profile. In the TW model, the effect of macromolecular relaxation is captured in a nonequilibrium contribution to the fluid's chemical potential, which is proportional to the local rate of dilation of polymer, the proportionality factor

---

[†] IBM Corporation, East Fishkill, NY 12533.

[‡] IBM Corporation, T. J. Watson Research Center, Yorktown Heights, NY 10598.

[®] Abstract published in *Advance ACS Abstracts*, May 1, 1995.

0024-9297/95/2228-4234$09.00/0 © 1995 American Chemical Society

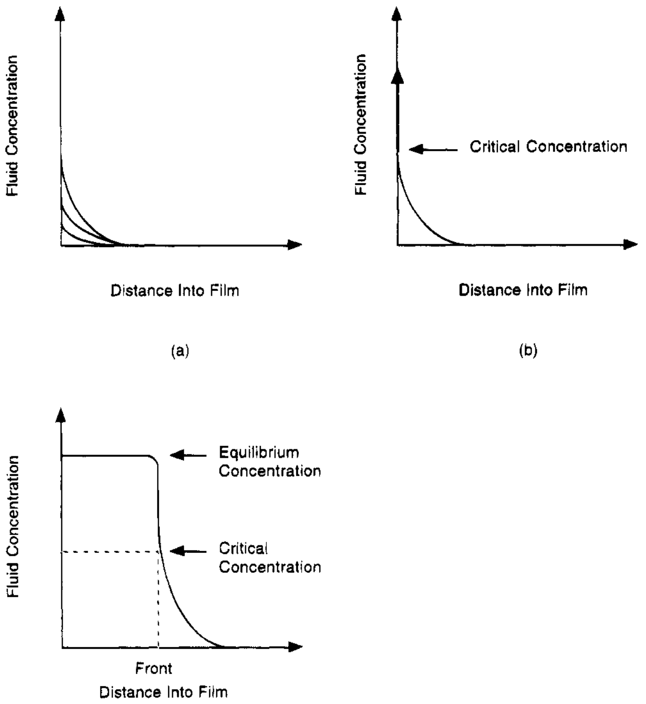

Figure 1. Schematic sequence illustrating development of Case II fluid concentration profiles during integral sorption: (a) induction; (b) front formation; (c) steady profile.

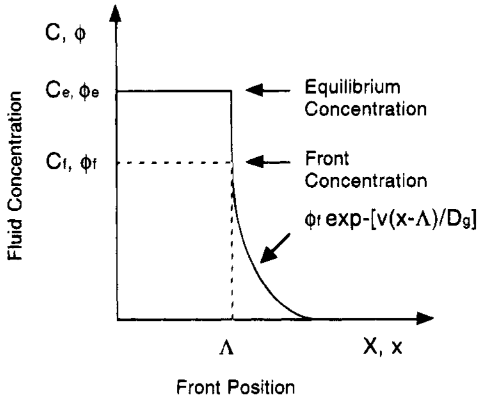

Figure 2. Schematic of step-exponential profiles predicted as asymptotic results from a modified Thomas and Windle model by Hui et al.[7,8] Here, C means the fluid concentration per unit polymer volume and ϕ means the fluid volume fraction. Also, X means the polymer material coordinate and x means laboratory coordinate.

being the local viscosity, η. Hui et al. assumed $\eta = \eta_0 \exp(-mC)$, where C is the local fluid concentration (per unit volume of polymer) and m is a constant. They also assumed a discontinuous diffusion coefficient: D was assumed to be constant, equal to D_g, for $0 < C < C_C$ where C_C is a critical concentration but to diverge for $C \ge C_C$. This key assumption, although idealized, enabled neat analytical solutions for two limiting cases; both are step-exponential profiles (Figure 2):

$$C(t,X) = \begin{cases} C_e & \forall X \in 0 \le X < \Lambda \\ C_f \exp\{-[v(X - \Lambda)/D_g]\} & \forall X \in \Lambda \le X \le l \end{cases}$$

$$\Lambda(t) \sim vt; \qquad v = \left(\frac{D_g RT}{\eta_0 V_1 \hat{V}_1}\right)^{1/2} \beta(m, C_e, C_C) \qquad (1)$$

Here, C_e is the equilibrium fluid concentration and C_f is the concentration at the moving front. X is the distance into the film in "polymer material" coordinates,[17] Λ is the position of the concentration front (Figure 2), and v is the speed of the front. Also, V_1 is the fluid's partial molar volume, $\hat{V}_1$ is the fluid's partial specific volume, R is the gas constant, and T is the absolute temperature.

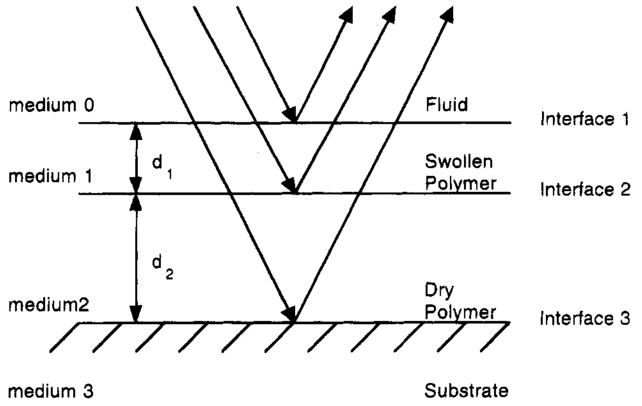

Figure 3. Schematic of multilayered system formed after immersion of polymer film into fluid.

The constant C_f and the value of the function β depend on the asymptotic case. When the viscosity decreases very strongly with fluid content ($mC_C \equiv M \gg 1$) and the velocity is large enough, $C_f = C_C$ and β is independent of C_e but has a complex dependence on m and C_C. The following condition judges the largeness of the velocity:

$$\frac{mD_g RT}{\eta_0 V_1 \hat{V}_1 v^2} \ll 1 \qquad (2)$$

The other asymptotic case obeying eq 1 is for slow fronts, defined by the group on the left in eq 2 being $\gg 1$. In this case $C_f = C_e$ and β obeys

$$\beta = \left(\frac{-\ln(C_C - C_e)}{C_C \exp(-mC_C)}\right)^{1/2} \qquad (3)$$

provided $mC_C \sim O(1)$.

The TW model does capture the essential characteristics of Case II and it has been studied in some detail. In the current study, we assume the step-exponential profile in the analysis of interferometry during Case II transport and adopt eq 1 as a basis for analyzing the effects of temperature and sample thermal history.

Interferometry

In this technique one measures the intensity of coherent, monochromatic light reflected at near-normal incidence from a multilayered film bounded on the top and bottom by semi-infinite media. The film of interest is a thin, supported, glassy polymer film undergoing Case II transport (Figure 3). The top medium (labeled with index 0) is the pure liquid while the bottom medium (index 3) is the substrate for the film. The film consist of two layers. The upper layer (index 1) corresponds to the swollen portion of polymer, and the lower layer (index 2) corresponds to the remaining dry, glassy polymer attached to the substrate; the two layers are separated by the Case II concentration front. The measured reflected intensity varies in time during Case II because the optical path length differences among reflections from the three interfaces vary as the front propagates into the film.

One can use the matrix method outlined in Appendix A to predict the reflected intensity from this structure. Appendix B summarizes two sets of calculations using this method to clarify the effects of the Case II characteristics on the reflected intensity signal. The first set of calculations predict the reflected intensity from the Case II front alone, R_{Tf}, assuming the step-exponential shape (eq 1). We find that a broad precursor ($\epsilon \equiv D_g/v > 0.2\lambda$; see eq 1 for D_g and v) of large amplitude ($C_f/C_e = \phi_f/\phi_e \sim O(1)$; see Figure 2 for ϕ_f and ϕ_e) renders the front completely ineffective in reflecting light: $R_{\mathrm{Tf}} \rightarrow 0$. The second set of calculations simulates the steady-periodic reflected intensity during Case II, $R_T(t)$, to show qualitatively how the real-time signal is affected by the volume fraction of liquid in the swollen portion behind the front, ϕ_e, the moving boundary speed, v, and the details of the step-exponential profile at the front.

The results of the second set of calculations in Appendix B are captured nicely by an analytical formula for R_T, derived using two approximations. First, the optical effect of the Case II front is approximated by putting

$$\mathbf{MF}_2 \sim \begin{bmatrix} e^{i\delta_1} & rf_2 e^{i\delta_1} \\ rf_2 e^{-i\delta_1} & e^{-i\delta_1} \end{bmatrix} \tag{4}$$

where $\mathbf{MF}_2$ is the transfer matrix characterizing reflection and transmission of light by the front (see eqs 20–24 in Appendices A and B). Here rf_2 is an effective reflection coefficient for the front and $\delta_j = 2\pi n_j(d_j/\lambda)$ gives the phase change for traversing layer j. Here n_j is the refractive index of medium j, d_j is the depth of layer j (see Figure 3 and eq 25 in Appendix B), and λ is the wavelength of the impinging light. Equation 4 ignores the phase shift introduced by the reflection from the Case II front. The second approximation used is to neglect all terms in the expression for R_T third order or higher in reflection coefficients (r_1, rf_2, r_3). This should be an excellent approximation since estimation shows that the interface reflectivities in the PMMA/MeOH system obey $r_1 \sim O(0.1) > r_3 \sim O(0.01) > r_2 \equiv rf_2 < O(0.01)$ (the reflectivities are labeled by the index of the medium below the interface; consequently, r_1 refers to the fluid/swollen polymer interface, rf_2 refers to the Case II front, and r_3 refers to the dry polymer/substrate interface).

Carrying out the manipulations indicated in eqs 20–24 of Appendices A and B leads to

$$R_T \simeq r_1^2 + r_2^2 + r_3^2 + 2r_1 rf_2 \cos 2\delta_1(t) + 2rf_2 r_3 \cos 2\delta_2(t) + 2r_1 r_3 \cos 2(\delta_1(t) + \delta_2(t)) \tag{5}$$

This relation shows that, in a first approximation, the interferometric signal is composed of three sinusoids superimposed on a mean value given by the sum of the intensities from each interface if isolated. Three distinct frequencies can be identified from the time dependence of the phase factors, $\delta_j(t)$ (see eq 25 of Appendix B and the definition of δ_j):

$$\omega_1 = 4\pi\frac{v}{\lambda}\left(n_{\mathrm{MeOH}}\frac{\phi_e}{1-\phi_e} + n_{\mathrm{PMMA}}\right)$$

$$\omega_2 = 4\pi\frac{v}{\lambda}n_{\mathrm{PMMA}}$$

$$\omega_3 = 4\pi\frac{v}{\lambda}n_{\mathrm{MeOH}}\frac{\phi_e}{1-\phi_e} \tag{6}$$

where n_{MeOH} and n_{PMMA} are the refractive indices of pure MeOH and PMMA, respectively. The first frequency is associated with interference between interfaces 1 and 2, the second with interfaces 2 and 3, and the third with interfaces 1 and 3. For typical cases involving PMMA/MeOH, the frequencies are ordered $\omega_1 > \omega_2 > \omega_3$. The corresponding amplitudes, $a_1 = 2r_1 rf_2$, $a_2 = 2rf_2 r_3$, and $a_3 = 2r_1 r_3$, are ordered $a_3 > a_1 > a_2$. The equations show that ϕ_e affects only ω_1 and ω_3, with the effect on the latter being more dramatic. These predictions agree perfectly with the results of more elaborate matrix-based numerical calculations discussed in Appendix B.

A quantitative comparison between eq 5 and the results in Appendix B was carried out to assess the error introduced by neglecting the phase change associated with reflection off the Case II front (interface 2). As the precursor became deeper, an obvious phase difference developed between the two predictions. However, the amplitude and frequency characteristics predicted by the approximation formula, eq 5, were in good agreement with the more exact numerical calculations. In what follows, we apply eq 5 to data with the *proviso* that phase information in the data be ignored.

Experimental Section

Materials. The system of interest is poly(methyl methacrylate) (PMMA) and methanol (MeOH). This system undergoes Case II transport under immersion conditions in the range 0–62 °C.[4] PMMA was obtained from Aldrich with (manufacturer specified) molecular weight $M_n = 46\,400$ and $M_w = 93\,300$. Semiconductor grade, anhydrous MeOH, obtained from Mallinckrodt was used for the majority of the experiments. For the preparation of PMMA solutions for film casting, reagent grade chlorobenzene was obtained from Aldrich. All of the above were used as received.

Two different substrates were used: $^1/_8$ in. thick, optical grade fused quartz plates (Thermal American Fused Quartz Co.) and 10 mil thick silicon (Si) wafers with an oxide coating (Virginia Semiconductor). Fused quartz (Qz) was chosen because its refractive index is close to that of solid PMMA ($n_{\mathrm{Qz}} = 1.458$; $n_{\mathrm{PMMA}} = 1.489$). This was done in an effort to reduce the reflectivity of the polymer/substrate interface (interface 3) as much as possible, thereby enhancing the influence of the reflection off the concentration front on the interferometric signal. Qz is transparent; therefore, thick plates were chosen to provide an effectively infinite substrate depth, i.e., to effectively eliminate the reflection off the back surface. In one set of runs, quartz plates with a sandblasted back surface, designated as QzS, were used to ensure complete elimination of back surface reflection. The silicon (Si) substrate ($n_{\mathrm{Si}} \simeq 3.8$) was chosen to create a situation where the polymer/substrate reflection is very strong as a contrast to the case of Qz. Si is a strongly absorbing medium at the wavelength of interest so the depth of the substrate is effectively infinite in this case.

Film Preparation. In the first set of experiments, designed to assess the effect of temperature on the Case II transport, solutions of 25–30 wt % PMMA in chlorobenzene were spin cast onto the substrate at 2000–3000 rpm. The coated substrates were first dried on a covered hot plate at 130 °C for about 60 min and then annealed at 80 °C for 24 h. The samples were immediately desiccated under vacuum (~0.1 Torr) at room temperature (~21 °C) for at least 24 h before use. This procedure effectively reduces the chlorobenzene content, provides a consistent thermal history for all samples, and prevents moisture from accumulating in the dried samples. For this set of experiments, the thickness of each dried

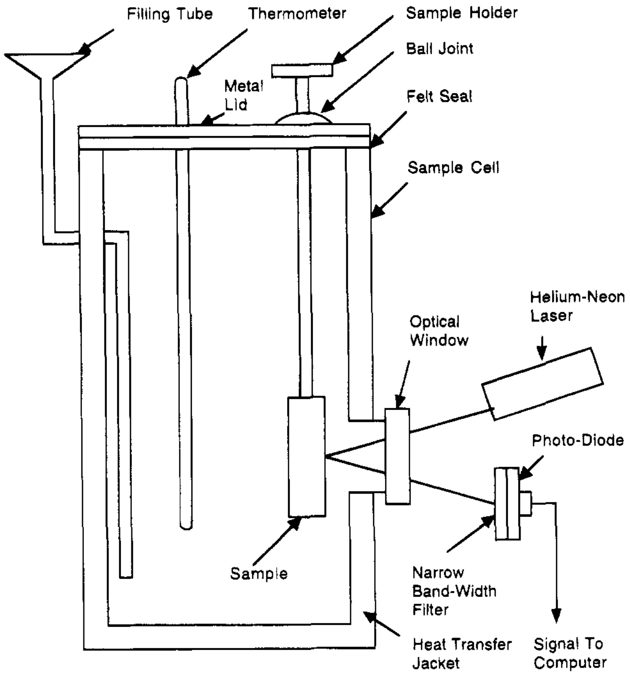

Figure 4. Schematic of interferometer.

Table 1. Cooling Rate from 130 °C through the Glass Transition Temperature (°C/s)

quench	to 114 °C	to 110 °C
a	30.3 ± 0.80	33.3 ± 0.80
b	2.86 ± 0.03	3.06 ± 0.03
c	2.25 ± 0.03	2.15 ± 0.03
d	1.90 ± 0.02	1.96 ± 0.02
e	0.019 ± 0.00	0.019 ± 0.00

specimen was determined by profilimetry before the interferometry. The dry film thicknesses were in the range of 1–9 μm depending on the solids content of the spinning solution and the precise spinning conditions employed.

In a second set of experiments, carried out to study the effect of the polymer film's thermal history on Case II, thin films were spin cast from solution onto the QzS substrates only. The coated substrates were then dried at 130 °C under vacuum ($\simeq$0.1 Torr) for 24 h and then quenched to below the glass transition temperature by one of five different methods:

(a) Fast quench: Molten samples were put directly into an ice/water slurry for 20 s.

(b) Cold vapor quench: Molten samples were put into a beaker surrounded with dry ice/acetone slurry for 2 min.

(c) Cold air quench: Molten samples were put into a beaker surrounded with an ice/water slurry for 2 min.

(d) Ambient air quench: Molten samples were removed, covered, and cooled on the lab bench at ambient conditions.

(e) Slow quench: Molten samples were kept in the vacuum oven and the temperature was gradually reduced.

After quenching, samples were immediately desiccated. The temperature history experienced by each sample was measured with a copper–constantan thermocouple attached to a Qz substrate. An average cooling rate was calculated for each quench from the linear regression slope of the measured initial temperature history; Table 1 summarizes the cooling rate data.

Apparatus and Procedure. The interferometer used (Figure 4) is very similar to that described in ref 18. The sample resides in a glass cell equipped with a quartz optical window. It is positioned in front of the window by an adjustable sample holder permitting alignment with the laser/photodiode. The temperature of the cell was controlled by circulating a thermostated ethylene glycol/water mixture through the cell's jacket. The controller provided ±0.1 °C regulation near the sample cell as determined by direct measurement with a thermocouple. A filling tube enabled the rapid admission of thermostated, liquid methanol to begin an experiment.

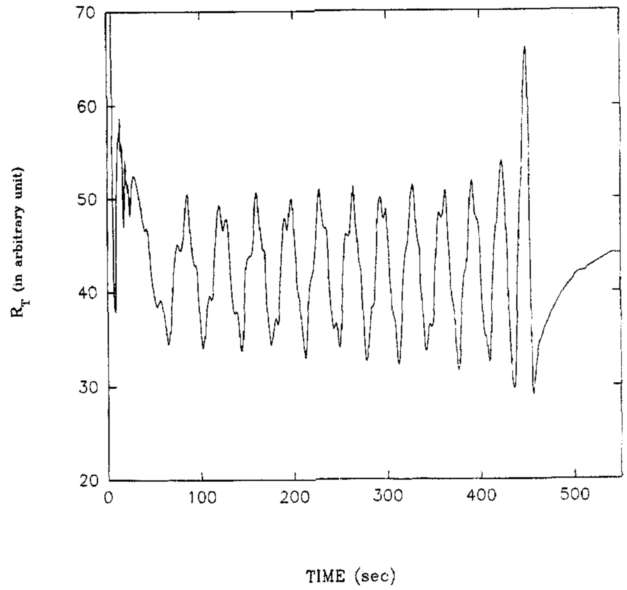

Figure 5. Real-time trace of R_T for a typical run (T = 30.5 °C; substrate = Qz).

A 1 mW helium–neon (He–Ne) laser (Spectra-Physics) provided unpolarized, monochromatic, coherent light (λ = 6328 Å). The laser was directed onto the sample at near-normal incidence (θ_0 < 5°). The reflected beam fell on a photodiode (United Detector Technology PIN 10 DP) set up in a photovoltaic mode. The photodiode was equipped with a narrow band filter (Oriel, peak wavelength = 6328 Å; bandwidth = 1 nm) to eliminate the effect of ambient light on the signal.

Two methods were used to read the voltage from the photodiode. In the first set of runs, exploring the effect of temperature, the signal was continuously recorded on a strip chart. Strip chart records were then converted to ASCII data files of voltage versus time using an x–y digitizer. The second set of experiments, studying the effect of thermal history, employed a data acquisition system based on a high-speed A/D interface board (MetraByte DAS-16). Digital data were acquired continuously at 10 Hz and stored on the computer hard disk for later analysis.

To run an experiment the sample was aligned in the empty cell and the baseline output with the laser on was recorded. The sample cell was then filled with thermostated methanol and the alignment of the sample was readjusted. The signal was recorded until a new baseline was established. At the end, the output with laser off was determined.

Results and Discussion

Qualitative Features. Figure 5 shows a typical run. The trace starts with a steady baseline from the reflection off the sample in an empty cell (not shown in Figure 5). The voltage drops suddenly at time t = 0 as soon as MeOH is added to immerse the sample. Filling often caused a shift in the position of the reflected beam on the photodiode, resulting in a drop of signal initially and requiring adjustment in the sample position to realign the beam with the photodiode. After realignment, a steady-periodic signal is soon observed: A low-frequency, large-amplitude oscillation with a higher frequency, smaller amplitude component superimposed. The steady-periodic trace was found to be very reproducible. Since the filling of the cell with methanol and subsequent realignment of the sample account for about 60 s, changes in R_T during the induction period of Case II (see Figure 1a) were not accurately recorded in this study.

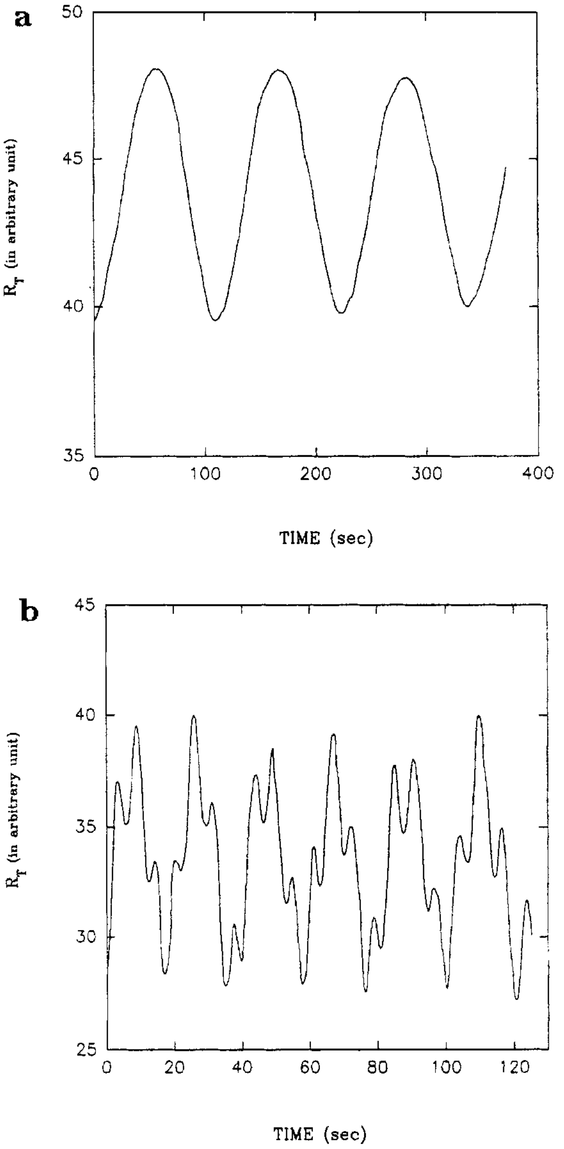

Figure 6. Steady-periodic part of real-time traces of R_T for typical runs on annealed samples: (a) ($T = 25.2$ °C; substrate = Qz); (b) ($T = 35.0$ °C; substrate = Qz). The time origin is arbitrarily set to zero.

Figure 6 compares two runs on annealed samples to show the qualitative effect of increasing temperature on the steady-periodic part of the signal. At the lower temperature of 25 °C (Figure 6a), the high-frequency component is absent, suggesting that the precursor at the front is tall and broad; i.e., $\phi_f/\phi_e \sim O(1)$ and $\epsilon/\lambda \geq 0.20$ at these conditions (see Figure 2). The data show three changes as the temperature increases (cf. Figures 6a and 6b): (i) the amplitude of the high-frequency component increases dramatically (the "shoulders" at 25 °C become prominent peaks at 35 °C with amplitude a large fraction of the low-frequency peaks), (ii) both the low and the high frequencies increase significantly, and (iii) fewer high-frequency peaks per large fringe are observed. In light of the modeling, the most likely explanations for each change are as follows: (i) as temperature increases, the height of the precursor drops (i.e., ϕ_f/ϕ_e falls from $\sim O(1)$ to a small value) and/or the width of the precursor drops (i.e., ϵ/λ decreases from ≥ 0.2 to $\ll 0.2$); (ii) the moving boundary velocity, v, increases significantly with temperature; (iii) the liquid fraction in the swollen layer, ϕ_e, increases significantly with temperature.

The last two trends are in perfect agreement with findings of Thomas and Windle.[4] Indeed, the quantitative analysis of our data discussed in the next section shows that both ϕ_e and v increase with temperature, with the increase in v being much more dramatic. The first suggestion remains somewhat equivocal, based on previous work. Using the RBS technique, Kramer and co-workers[5-10] did observe a precursor in several systems; they found its height, ϕ_f/ϕ_e, was not a strong function of temperature in the systems Riston (cross-linked PMMA)/trichloroethane and polystyrene/iodohexane. This seems to favor the explanation that the precursor's width, ϵ/λ, falls with temperature. Unfortunately, the idea is not completely supported by their other findings: For the polystyrene/iodohexane system ϵ indeed decreases with temperature, but the trend is very weak and in the Riston/trichloroethane system ϵ was found to be independent of temperature over a wide range of temperatures. We will return to this point subsequently.

The qualitative effects of the polymer film's thermal history on the Case II transport are illustrated by comparing several runs at one temperature on quenched samples made with different quenches. The following changes were observed with the increasing quench rate: (i) the amplitude of the high-frequency component decreases (the effect is prominant only at the highest cooling rate); (ii) the low frequency increases sharply, by approximately a factor of 3 for each order of magnitude increase in cooling rate; (iii) the number of high-frequency peaks per large fringe remains roughly unchanged. In light of the modeling in Appendix B, the most likely explanations for these changes are (i) the height and depth of the precursor at the Case II front, i.e., ϕ_f/ϕ_e and ϵ/λ, are sensitive to the quench procedure, especially at the higher cooling rates, (ii) the moving boundary velocity increases significantly with increased cooling rate, and (iii) ϕ_e does not change with the sample's cooling rate. The last two explanations are consistent with a detailed quantitative analysis presented in the following section. Regarding the first trend, it is interesting to note that it corresponds to a completely different behavior of the Case II front than was observed in the first series of experiments on annealed samples. These revealed that the sharpness of the front *increases* along with the front velocity. Here, where the polymer film's thermal history is varied, the sharpness *decreases* as the front velocity increases. Since ϕ_e does not change with the cooling rate, it must be an increase in ϕ_f and/or ϵ with quench rate which is responsible for the decrease in sharpness of the front in quickly quenched samples. For the latter to be true, the diffusion coefficient, D_g, must increase more than the front velocity, v, when the sample is quenched more quickly (recall, the front's width is $\epsilon = D_g/v$). We will return to this point subsequently.

Quantitative Analysis. The approach taken for quantitative analysis is to calculate the power spectrum of the steady-periodic portion of the signal by Fourier transform. The spectrum clearly reveals the dominant frequencies from the location of spectral peaks; these are interpreted using eqs 6. The corresponding peak heights give the products of the reflectivities indicated in eq 5. The advantage of this approach is that is relies only on the steady-periodic portion of the signal and does not depend on the phase information in the data.

For each run, the steady-periodic signal, $R_T(t)$, was discretized to give samples R_{Tk}, evenly spaced in time.

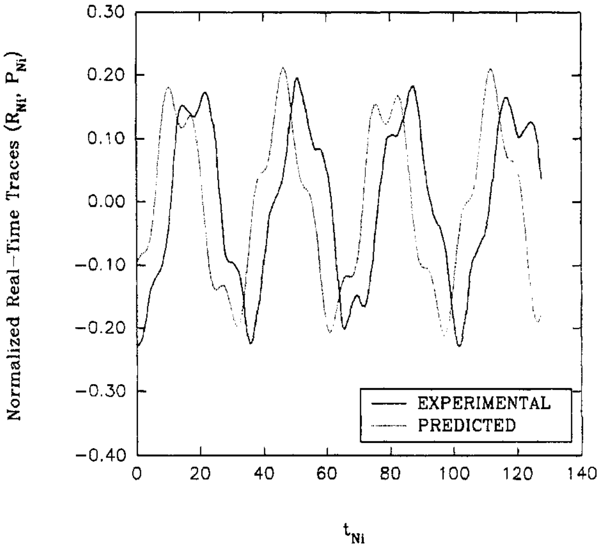

Figure 7. Comparison of normalized real-time trace, R_{Ni} (solid curve), and trace predicted from eq 5, P_{Ni} (dotted curve), with parameters corresponding to the model spectrum in Figure 8.

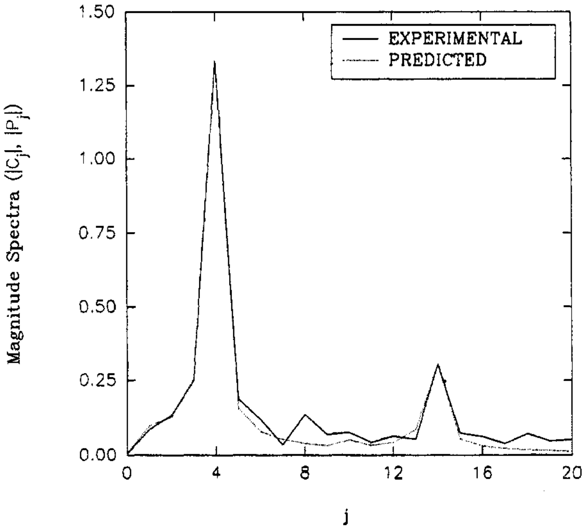

Figure 8. Comparison of actual (solid line) and model (dotted line) magnitude spectra for a typical run on annealed samples (T = 30.5 °C; substrate = Qz) after adjustment of model parameters.

The data set was then normalized according to

$$R_{Nk} = \frac{R_{Tk} - M}{M} \qquad (7)$$

where M is the mean calculated by numerical integration of the R_{Tk}. The normalized data, R_{Nk}, were then Fourier transformed by the algorithm of Sande and Tukey.[19] The interpretation of the discrete Fourier transform cannot be made directly in terms of eq 5 without compensation for discretization and "leakage" errors.[19] To account for these, numerical values of R_{Nk} were predicted from eq 5 over the same time interval and a model power spectrum was calculated. The parameters ϕ_e, v, and rf_2 were varied by trial to produce a good match between the actual and model spectra.

To illustrate the fitting process, consider results from a typical run (annealed sample, T = 30.5 °C; Qz substrate). Figure 8 shows the power spectrum of the normalized data appearing in Figure 7 (solid lines). The quantity C_j is

$$C_j = \frac{1}{n^{1/2}}\sum_k R_{Nk} \exp\left(2\pi i \frac{j}{n} k\right) \qquad (8)$$

where n (=256) is the size of the data array. The final model results also appear (dotted lines). Except for the difference in phase, the model reproduces the real-time data accurately. The parameters deduced from the fit correspond well with published results. The equilibrium volume fraction, ϕ_e, from Figure 8 is found to be 0.30, which is ≃10% larger than that reported by Thomas and Windle[4] at the same conditions; the front velocity, v/λ = 0.026 Hz or 0.059 mm/h, is also of reasonable magnitude, although about 2.5 times that reported by Thomas and Windle. The differences could have resulted from the difference in polymer molecular weight (93K [illegible] 4000K in Thomas and Windle's) or the [illegible] ion procedures (spin casting and anne[illegible] ymerization). The value of the front's reflectivity in this case (−0.00085) is considerably smaller than that from the Fresnel formula for a true discontinuity (−0.017).

A sensitivity analysis was performed to determine the typical uncertainties in the model parameters. We used the following procedure for this. First, we determined ϕ_e, v, and rf_2 giving the best visual match between the actual and model spectra. Then, with two parameters fixed, we varied the third to determine the limiting values for which the fit became visually unacceptable. The typical uncertainty in ϕ_e determined for runs on annealed samples is ±0.01 for all temperatures examined. The corresponding uncertainty in v is ±0.001 Hz for runs below 25 °C and ≃±0.003 Hz for higher temperatures. The uncertainty in rf_2 is large at low temperatures (≤25 °C) because the high-frequency component is only a weak contribution or is completely absent. For these conditions we report a maximum value of rf_2 although values below this gave reasonable representations of the data. For runs at higher temperatures (>25 °C) uncertainties in rf_2 are ~±0.0001.

Effect of Substrate. For runs on annealed samples we found that the values of ϕ_e and v deduced via FFT were independent of the substrate but that the value of rf_2 does depend on the substrate. In particular, use of the QzS substrate always resulted in significantly higher values of $|rf_2|$ than for the Qz substrate. Since the back surface of the QzS substrates were sandblasted, which completely eliminates the influence of a back surface reflection, the rf_2 found for these cases are considered more accurate than those found from samples on Qz. This observation motivated using only QzS substrate on quenched samples so as to obtain the best possible values of rf_2 as a function of temperature.

Data from the Si substrate yielded values for ϕ_e and v within 10% of those from Qz and QzS substrates, for all temperatures. However, because of the much higher reflectivity of the polymer/substrate interface, the high-frequency peaks associated with reflection from the liquid front were almost completely obscured. Accurate determination of rf_2 in such cases was practically impossible.

Effect of Temperature in Annealed Samples. Figure 9 shows the dependence on temperature of ϕ_e, the equilibrium methanol volume fraction for the runs on annealed samples. It increases with temperature by a factor of about 2 over an interval of approximately 30 °C, from about 0.2 at 20 °C to about 0.4 at 52 °C. The magnitude and trend closely follow those determined

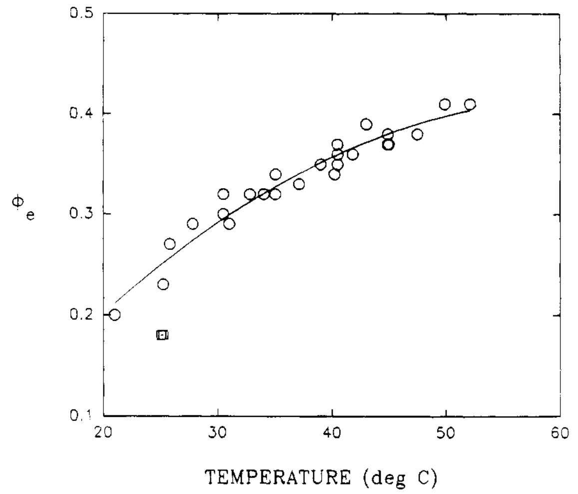

Figure 9. Dependence of equilibrium volume fraction of methanol, ϕ_e, on temperature for the experiments on annealed samples.

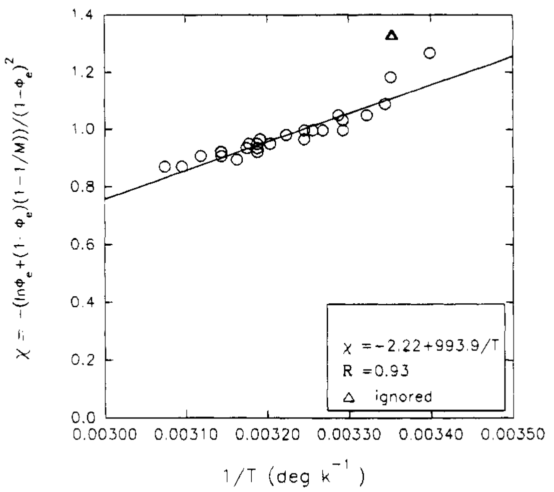

Figure 10. Dependence of Flory–Huggins interaction parameter, χ, on temperature for the data from Figure 9. The linear regression coefficient for the fit is $R = 0.93$.

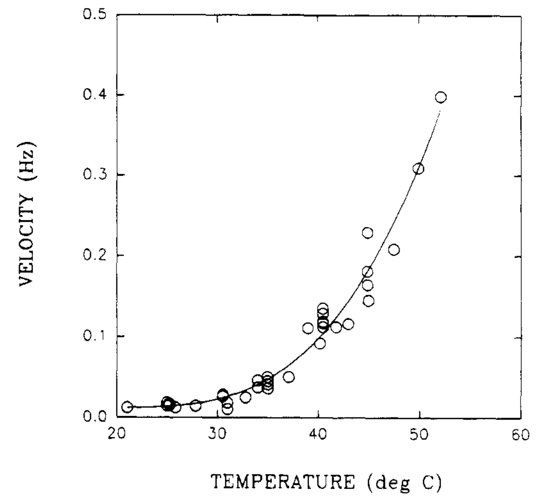

Figure 11. Dependence of front velocity, v/λ, on temperature for experiments on annealed samples.

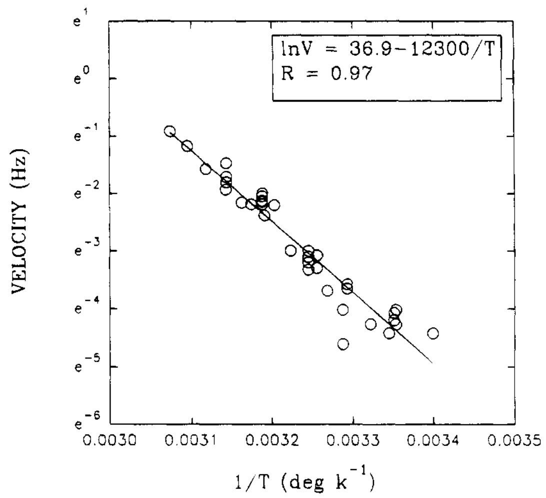

Figure 12. Arrhenius plot of the front velocity, v/λ, for experiments on annealed samples. The linear regression coefficient for the fit is $R = 0.97$.

by Thomas and Windle[3,20] by a completely different, macroscopic method.

For a thermodynamic interpretation of ϕ_e, consider the Flory–Huggins solution theory, which gives the equilibrium condition

$$\ln \phi_e + \left(1 - \frac{1}{M}\right)(1 - \phi_e) + \chi(1 - \phi_e)^2 = 0 \qquad (9)$$

under immersion conditions. Here, M is the degree of polymerization of the polymer ($M \sim O(10^3-10^4)$) and χ is the interaction parameter. χ is usually found to be temperature dependent, often obeying the simple relationship $\chi = A + B/T$. If ϕ_e determined from the interferometry truly corresponds to the equilibrium volume fraction, then a plot of $-(\ln \phi_e + (1 - 1/M)(1 - \phi_e))/(1 - \phi_e)^2$ vs $1/T$ should yield a straight line. Figure 10 shows the plot; the linear fit is quite reasonable. At 24 °C, χ is found to be 1.1, close to the value of 1.0 reported by Thomas and Windle.[16] The plot indicates that χ exceeds $1/2$ for temperatures up to 90 °C, far beyond the temperature range used in our experiments. It correctly reflects that the polymer only swells and does not dissolve into methanol over the temperature range examined.

The Case II front velocity for annealed samples, expressed as v/λ (Hz), appears in Figure 11. The experiments span a temperature range of approximately 30 °C. v increases by a factor of about 3.5 from 20 to 35 °C and by a factor of about 7 from 35 to 50 °C. The roughly exponential increase in v with temperature is unusually strong and not characteristic of pure diffusion processes.

An Arrhenius plot of the velocity data (Figure 12) gives the apparent activation energy, E_{Arr}, of 24.5 ± 1.1 kcal/mol (with 95% confidence), somewhat below the 25–27.5 kcal/mol reported by Thomas and Windle.[4,20] According to the analysis of Thomas and Windle's model by Hui et al.,[7,8] $v \sim (D_g T/\eta_0)^{1/2}$ (see eq 1) so that $E_{\mathrm{Arr}} \simeq (E_\eta + E_D)/2$, where E_η and E_D are the apparent activation energies for viscous flow of the dry polymer and for diffusion of a trace of the fluid in the dry polymer, respectively. By comparing numerical solutions of their model with Case II sorption data, Thomas and Windle[16] concluded $E_D \simeq 14$ kcal/mol and $E_\eta \simeq 28.3$ kcal/mol in the PMMA/MeOH system, which yields E_{Arr} of 21.2 kcal/mol, below their experimental values. Subsequently, we present calculations of E_D and E_η using the free-volume theory and find much different values than those reported in ref 16.

The very nice fit of the data by the Arrhenius relation suggests that the front motion is energy controlled. However, it is well known that for relatively small temperature intervals rate processes governed by free volume also yield a nearly straight line in an Arrhenius plot. Therefore, we analyzed the v vs T data on the basis of the free-volume theory, in the form proposed by Vrentas and Duda,[21-29] to explore whether a free-volume description can capture the trend in v vs T.

According to Vrentas and Duda, the following relationships apply in the limit of zero liquid concentration for temperatures $T < T_{g2}$, where T_{g2} is the glass transition temperature of the dry polymer:

$$D = D_1 = D_{01} \exp\left[-\frac{\gamma \hat{V}_2^* \xi}{\hat{V}_{\mathrm{FH}_2}}\right] \qquad (10)$$

$$\eta_0 \sim \frac{1}{D_2} = \eta_\infty \exp\left[\frac{\gamma \hat{V}_2^*}{\hat{V}_{\mathrm{FH}_2}}\right] \qquad (11)$$

$$\hat{V}_{\mathrm{FH}_2} = k_{12}\lambda\left(\frac{k_{22}}{\lambda} + T - T_{g2}\right) \qquad (12)$$

where D is the mutual diffusion coefficient of the polymer/fluid system, D_1 is the self-diffusion coefficient of the fluid, and η_0 is the zero-shear rate viscosity of the polymer. D_{01} and η_∞ are pre-exponential constants, $\hat{V}_{\mathrm{FH}_2}$ is the average specific free volume, γ is a dimensionless overlap factor ($^1/_2 \le \gamma \le 1$), and the quantity ξ is the ratio of the "critical" molar volume of the fluid ($\tilde{V}_1^*$) to that of the polymer "jumping" units ($\tilde{V}_2^*$), i.e.

$$\xi = \frac{\tilde{V}_1^*}{\tilde{V}_2^*} = \frac{\hat{V}_1^* M_1}{\hat{V}_2^* M_j} \qquad (13)$$

where M_1 is the molecular weight of the solvent and M_j is the molecular weight of the polymeric jumping unit. The $\tilde{V}_i^*$ in eq 13 give the (molar) volumes required for a diffusive displacement of this component's jumping unit (subscripts 1 and 2 refer to the fluid and polymer, respectively).

The quantities k_{12} and k_{22} are related to the WLF constants of the polymer, $(C_1^g)_2$ and $(C_2^g)_2$, by

$$\frac{\gamma \hat{V}_2^*}{k_{12}} = 2.303 (C_1^g)_2 (C_2^g)_2 \qquad (14)$$

$$k_{22} = (C_2^g)_2 \qquad (15)$$

The parameter λ is, roughly, the ratio of the thermal expansion coefficient of the pure polymer below T_{g2} to that above T_{g2} which lies below a well-defined upper limit for a given polymer. A detailed discussion of the free-volume theory used in this work appears in refs 21–29.

For the temperature range used in our experiments, we assume β, V_1, and $\hat{V}_1$ in eq 1 remain constant; hence from eqs 1, 10, and 11 we get

$$\ln(v/T^{1/2}) = -\frac{1}{2}\frac{\gamma \hat{V}_2^*}{k_{12}}(1 + \xi)\frac{1}{\lambda(k_{22}/\lambda + T - T_{g2})} + \text{const} \qquad (16)$$

If the free-volume theory correctly represents the system's behavior, then a plot of $\ln(v/T^{1/2})$ vs $1/\lambda(k_{22}/\lambda + T - T_{g2})$ should yield a straight line with slope equal to $(-1/2)(\gamma\hat{V}_2^*/k_{12})(1 + \xi)$. To do the plot, we used the (manufacturer specified) value of T_{g2} = 105 °C for PMMA. Since the value of λ depends on the thermal history of the sample, we kept it as a fitting parameter, varying it such that the slope of the plot matches the expected theoretical value. The slope expected was determined as follows: The value of $\gamma\hat{V}_2^*/k_{12}$ was determined from eq 14 with $(C_1^g)_2 = 35.32$ and $(C_2^g)_2 = 77$ °K, obtained from ref 30 after proper adjustment of the reference temperature. The quantity ξ was calculated from eq 14 and a value of $\gamma\hat{V}_2^*\xi/k_{12} = 423$, derived from the correlation in Figure 6 of ref 28, and was found to be 0.0675.

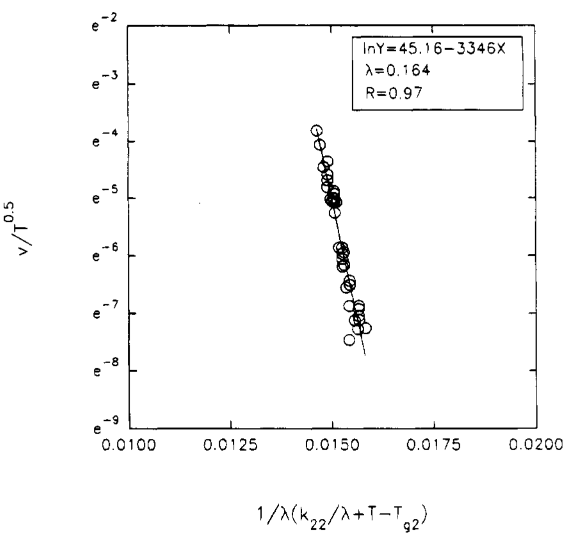

Figure 13. Dependence of the front velocity, v/λ, on free-volume for experiments on annealed samples. The linear regression coefficient for the fit is R = 0.97.

The plot appears in Figure 13. An excellent fitting of the data indicates that the free-volume theory nicely describes the temperature dependence of v in annealed samples. The parameter λ was found to be 0.164, which is well below the upper limit for PMMA of 0.41 discussed in ref 25. To check the value of λ, we used an alternate plot, suggested in ref 25,

$$\ln\frac{v}{T^{1/2}} = \frac{1}{2}\frac{\gamma\hat{V}_2^*}{k_{12}k_{22}}(1 + \xi)\left[\frac{T - T_{g2}}{k_{22}/\lambda + T - T_{g2}}\right] + \text{const} \qquad (17)$$

Using the same value of λ, we expect to get a slope of $(1/2)(\gamma\hat{V}_2{}^*/k_{12}k_{22})(1 + \xi)$ from a plot of $\ln(v/T^{1/2})$ vs $(T - T_{g2})/(k_{22}/\lambda + T - T_{g2})$. It is clear from Figure 14 that the slope is indeed equal to the theoretically expected one confirming the value of λ. Clearly, the free-volume theory describes the temperature dependence of v in annealed samples very well.

Consider the apparent activation energy for v according to the free-volume theory, E_{Eff}. We calculated the individual activation energies, E_{D} and E_η from the relations[25]

$$E_{\mathrm{D}} = \frac{RT^2 \dfrac{\gamma\hat{V}_2^*\xi}{\lambda k_{12}}}{(k_{22}/\lambda + T - T_{g2})^2}$$

$$E_\eta = \frac{RT^2 \dfrac{\gamma\hat{V}_2^*}{\lambda k_{12}}}{(k_{22}/\lambda + T - T_{g2})^2}$$

Then

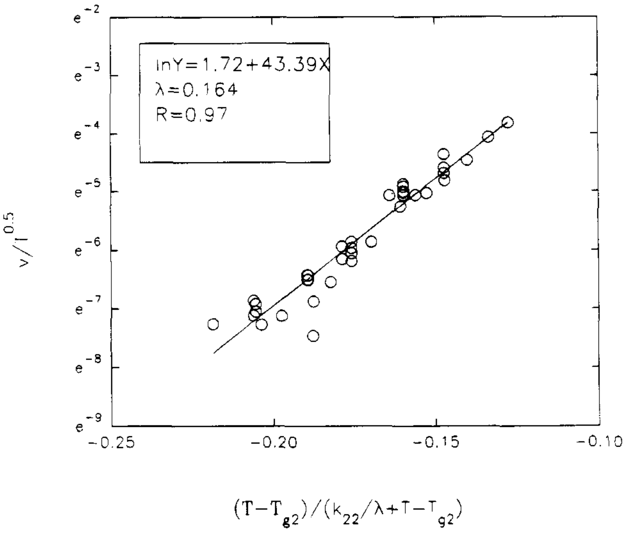

Figure 14. Alternate plot of dependence of the front velocity, v/λ, on free-volume for experiments on annealed samples; the line has the slope $(1/2)(\gamma\hat{V}_2^*/k_{12}k_{22})(1+\xi)$. The linear regression coefficient for the fit is $R = 0.97$.

$$E_{\mathrm{Eff}} = \frac{E_{\mathrm{D}} + E_\eta}{2} \tag{18}$$

Over the temperature interval of interest (20−55 °C), the apparent activation energies from free volume theory increase weakly, by about 5%. The average value for the interval is $E_{\mathrm{Eff}} = 24.3$ kcal/mol, in agreement with Figure 12. We find $E_{\mathrm{D}} \simeq 3.1$ kcal/mol, about 5 times less than that deduced by Thomas and Windle (14 kcal/mol). The calculated value of $E_\eta \simeq 45.4$ kcal/mol is far larger than Thomas and Windle's estimate by approximately a factor of 1.6. Viscous flow of the polymer matrix clearly dominates the temperature dependence of v.

Figure 15 shows the effect of temperature on the Case II front's reflectivity, rf_2, for annealed samples on quartz substrates. At low temperatures the value is close to zero for all substrates, indicating that the Case II front is not very sharp; i.e., the main change in the liquid content at the front occurs over a spatial scale greater than 0.2λ. With increasing temperature, $|rf_2|$ increases at first with the gradient depending on the substrate. As discussed earlier, $|rf_2|$ for QzS substrates were highest and we assert that these values are the most accurate.

Even on QzS substrates, significantly smaller values of rf_2 than for a true discontinuity were found for the whole temperature range, revealing the presence of a finite width to the front on the order of 0.2λ. The initial increasing trend of rf_2 with temperature indicates that the concentration front moves toward a true discontinuity with increasing temperature. In the context of the step-exponential model for the front, three explanations are possible for this behavior: As the temperature increases, (i) the precursor height, ϕ_f/ϕ_e, drops to $\phi_f/\phi_e \ll 1$, (ii) the precursor width, ϵ, shrinks to $<0.2\lambda$, or (iii) a combination of (i) and (ii) occurs. That ϕ_f/ϕ_e and ϵ decrease with temperature is perfectly consistent with eq 1 in the "fast front" limit. We know that ϕ_e monotonically increases with temperature (Figure 10). The physical interpretation of ϕ_f for the fast front asymptote, the liquid fraction depressing the glass transition to the experimental temperature, indicates that ϕ_f decreases with increasing temperature. Hence ϕ_f/ϕ_e should decay monotonically with temperature, increasing the step portion of the profile and enhancing rf_2. At the same time ϵ should fall monotonically with temperature since $\epsilon \sim D_g/v \sim (D_g\eta_0)^{1/2} \sim \exp[(E_\eta - E_{\mathrm{D}})/RT]$, and the factor $E_\eta - E_{\mathrm{D}}$ is predicted by free-volume theory to be positive over the whole temperature range studied in this system.

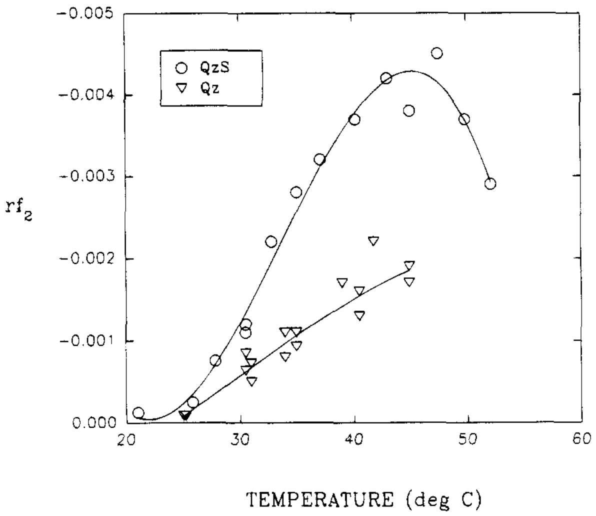

Figure 15. Effect of temperature and substrate on the front reflectivity, rf_2 for experiments on annealed samples.

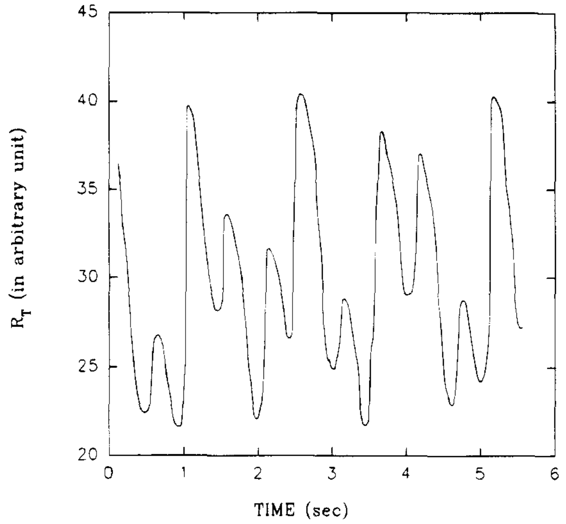

Figure 16. Steady-periodic part of the real-time trace of R_{T} for a run at $T = 52.1$ °C on an annealed sample.

Presuming that the reflectivities from QzS substrates are the most reliable, it is interesting to note that $|rf_2|$ passes through a maximum at around 45 °C. It indicates that, although the front becomes sharper with increasing temperature at first, with increases in temperature beyond 45 °C the front loses sharpness. Now, Thomas and Windle[4] reported that Case II becomes limited by the diffusion of the liquid in the swollen portion behind the front at about 60 °C for methanol in thick (1 mm) PMMA plates. If this were reponsible for the decrease in $|rf_2|$ beyond 45 °C, we should also observe the signature of the diffusion-controlled front motion, that the low-frequency sinusoid's period increases with time; i.e., the signal would be stretched. Figure 16 shows the steady-periodic part of the signal at 52.1 °C for times when nearly half the diffusion process is completed. The signal is composed of evenly spaced low-frequency fringes, making it clear that for all temperatures used in our experiments the front moves at constant speed; i.e., the transport process

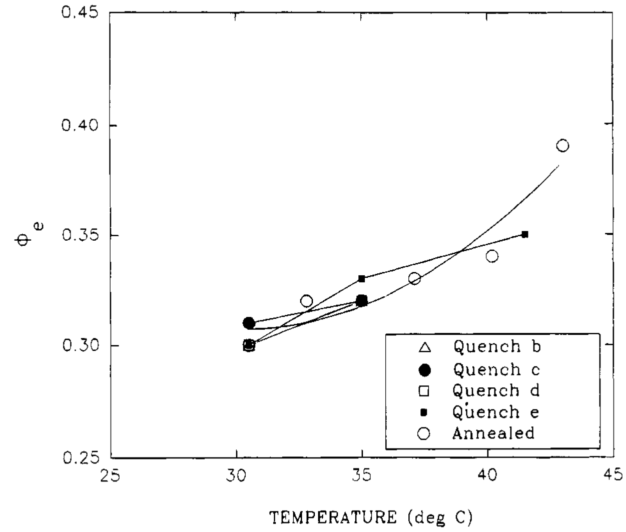

Figure 17. Effect of polymer sample's thermal history on the equilibrium volume fraction of methanol, ϕ_e, in quenched samples.

was pure Case II and not influenced by diffusion in the swollen layer. This is expected since the films employed in our study are 100−1000 times thinner than those used in Thomas and Windle's, relieving any diffusion limitation of the front motion.

One cannot explain the maxima in $|rf_2|$ by changes in the step-exponential profile's precursor depth, ϵ, with temperature since the factor (E_η − E_D) is positive over the whole temperature range for the annealed samples. One can possibly think that ϕ_f/ϕ_e increases significantly in the upper portion of the temperature range; however, this is contrary to the predictions of Hui et al.'s analysis,[7,8] which indicates smaller values of ϕ_f/ϕ_e accompany an increase in v, making ϕ_f/ϕ_e a strictly decreasing function of temperature. Hence, the expected trends in ϵ and ϕ_f/ϕ_e should turn the front reflectivity to ever larger values with increasing temperature, which is not the case. So the reason for the maximum in rf_2 is not clear at this point.[37]

Effect of Thermal History in Quenched Samples. QzS substrates were used for all runs on quenched samples. The equilibrium volume fraction, ϕ_e, was found to be independent of the sample's thermal history and increasing with temperature, as found in annealed samples. Both of these facts are revealed in Figure 17.

Figure 18 presents the Case II front velocity as a function of temperature for samples with different thermal history. It is clear from the figure that at the same temperature faster quenched samples have a higher diffusion velocity. For example, at 30.5 °C, increasing the cooling rate through T_{g2} by 3 orders of magnitude increases the velocity by an order of magnitude. The effect is much stronger than that observed by Windle.[31] The results are not surprising. It is well understood that the more rapidly a noncrystalline polymer is cooled through its glass transition temperature, the lower is the density of the resulting glass. This suggests greater free volume is trapped in the glass. According to eq 1, increased free volume enhances v by decreasing the viscosity, η, and increasing the diffusion coefficient, D_g.

We followed the same procedures as in the previous section to analyze the data for this set of experiments. First, we determined the effective activation energies from the Arrhenius model; Table 2 summarizes the results (last row). Since only two temperatures were examined for samples prepared with quenches b, c, and d, and three points for samples prepared with quench e, one should consider the calculated E_{Arr} as estimates only. The apparent activation energy for v increases from 22 kcal/mol for quench b samples (highest cooling rate) to 31 kcal/mol for quench e samples (lowest cooling rate). Evidently, the apparent activation energy depends on the thermal history of the polymer samples, increasing with decreasing cooling rate through T_g. Presumably, faster cooling traps more free volume into the glass, yielding a lower apparent activation energy.

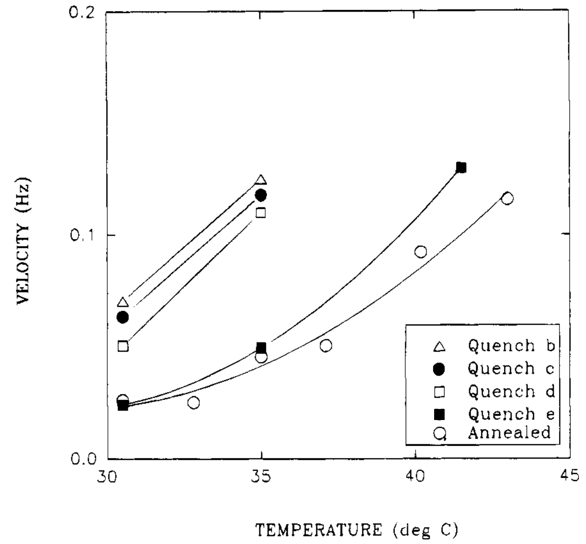

Figure 18. Effect of polymer sample's thermal history on the front velocity, v/λ, in quenched samples.

Table 2. Activation Energies at 30.5 °C for Experiments on Quenched Samples

		quench			
model	E (kcal)	b	c	d	e
free-volume	E_D	2.9	3.4	4.0	3.9
variable	E_η	42.5	50.7	59.7	57.6
λ, T_{g2}	$E_\eta - E_D$	39.6	47.3	55.7	53.7
	E_{Eff}	22.7	27.1	31.9	30.8
Arrhenius[a]	E_{Arr}	22	26	31	31

[a] Estimates based on data at two or three temperatures.

In a first attempt to quantitatively analyze the effect of thermal history on v, we repeated Thomas and Windle's calculations[20] by plotting the front velocity against the logarithm of the cooling rate; Figure 19 shows the result for the front velocities measured at 30.5 °C. The linear regression fit of the data is barely acceptable (correlation coefficient R = 0.85). Parenthetically, Thomas and Windle[20] reported an excellent fitting in a plot of sorption rate vs logarithm of cooling rate for this system.

To improve the quantitative interpretation, we applied the Vrentas and Duda free-volume theory to analyze the data. Consider the factors that determine changes in free-volume when varying the quench rate through T_{g2} of a polymer sample. From eq 12, T_{g2} is clearly an important factor which changes with cooling rate.[33] One should note that a change in T_{g2} alters k_{22}, since k_{22} corresponds to $(C_2^g)_2$, the WLF constant of the polymer which depends on the reference temperature. (Since k_{12} corresponds to the product $(C_1^g)_2(C_2^g)_2$, which is independent of any reference temperature, it remains unchanged.) The other factor which might be affected by the cooling rate is λ.

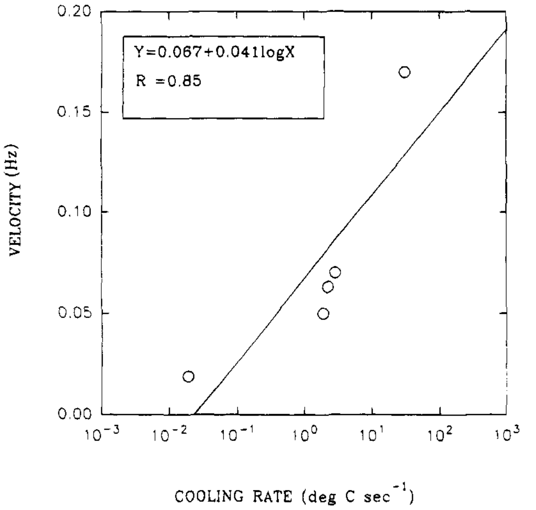

Figure 19. Dependence of front velocity, v/λ, on polymer sample's quench rate through the glass transition temperature, T_{g2}. The linear regression coefficient for the fit is $R = 0.85$.

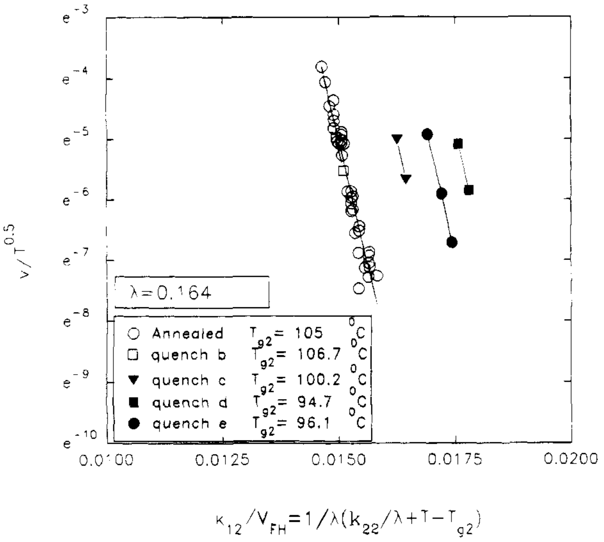

Figure 20. Dependence of the front velocity, v/λ, on free volume for samples with different thermal history. The parameter λ was held constant at 0.164 for the fits.

In a first attempt to apply the free volume theory, we used the same procedure as in Figure 13 with fixed $\lambda = 0.164$ obtained from the analysis of the temperature dependence of annealed samples, assuming it independent of cooling rate. We varied T_{g2}, and accordingly k_{22}, to get the correct theoretical slope. Figure 20 shows the result. With one exception (quench e), the glass transition temperatures obtained in this fashion were consistent with the expectation that higher cooling rates result in a higher T_{g2}. It is known that a change in cooling rate by an order of magnitude ([=]°C/s) brings about a 3 °C change in T_{g2}.[33] The values obtained by Figure 20 did not obey this rule; the predicted change in T_{g2} is much larger. Moreover, if free-volume alone determines v and all the underlying assumptions made in applying the free-volume theory are valid, then all the data of Figure 20 should collapse onto a single line in a plot of $\ln(v/T^{1/2})$ vs reciprocal of free-volume (since k_{12} is constant, $k_{12}/\hat{V}_{FH} = 1/[\lambda(k_{22}/\lambda + T - T_{g2})]$ is simply a rescaling of $1/\hat{V}_{FH}$). It is clear from Figure 20 that the data do not collapse onto a single line. Only one pair of data sets coincide, quench b and the data for annealed samples, while all other sets, corresponding to different coooling rates, are well separated from the each other.

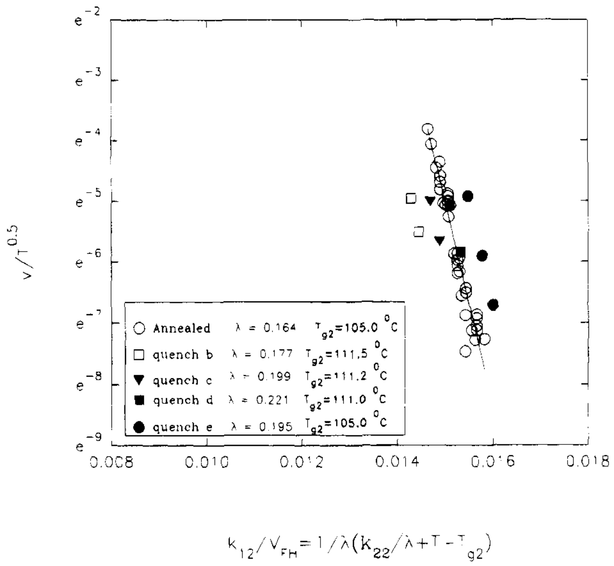

Figure 21. Dependence of the front velocity, v/λ, on free volume for samples with different thermal history. Both parameters λ and T_{g2} were varied for the fits; see text for details.

In a second attempt, we fixed the T_{g2} at 105 °C and repeated the same procedure, this time varying λ to obtain the theoretical slope. This approach produced much better results. All of the lines fell relatively close to each other compared to those in Figure 20. Further, the λ appeared to be in correct order. If T_{g2} is considered constant, then an increased cooling rate results in higher free volume by a decreased thermal expansion coefficient of the glassy polymer. Consequently, λ should decrease with increasing cooling rate; the values of λ determined by fitting with fixed T_{g2} followed this trend.

The above two attempts to fit the data suggest that proper selection of both T_{g2} and λ could produce a universal plot of $\ln(v/T^{1/2})$ against inverse free-volume. In an attempt to demonstrate this, we assigned T_{g2} = 105 °C for both annealed and the slowest quench samples (quench e) and increased T_{g2} by 3 °C for each order of magnitude increase in cooling rate. λ was then found as before. The results are shown in Figure 21. Now the plots for all samples cluster close together. We conclude that to a good approximation there exist systematically varying combinations of T_{g2} and λ for which all the lines collapse into one single line.

Based on the results in Figure 21 we calculated the various activation energies for quenched samples; Table 2 shows the results for 30.5 °C. It is interesting to note that both E_D and E_η increase with decreasing cooling rate. This makes perfect sense in the context of free-volume theory: Slow quenched samples contain less free volume; hence the relative effect of temperature is greater. The effective activation energies for v predicted from free-volume theory vary from approximately 23 to 32 kcal/mol with sample cooling rate, which follows the trend calculated directly from the data by the Arrhenius model.

Finally, consider the effect of thermal history on the Case II front's reflectivity. Figure 22 shows the front reflectivity, $|rf_2|$, as a function of temperature for samples prepared with different quench procedures. It is evident from the figure that rf_2 strongly depends on the sample's thermal history: It decreases with increasing cooling rate of the samples through T_{g2}. For all temperatures, the $|rf_2|$ of the annealed samples were an

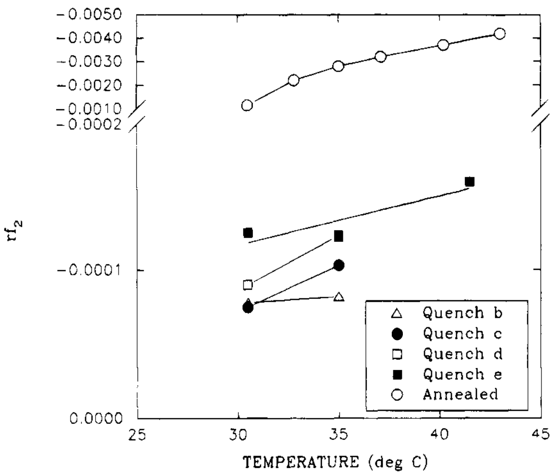

Figure 22. Effect of polymer sample's thermal history on the front reflectivity, rf_2.

order of magnitude higher than for quenched samples. As mentioned in a previous section, if one adopts the step-exponential model for the front's shape, the reduction in $|rf_2|$ with increased sample quench rate must correspond to an increase in ϕ_f/ϕ_e and/or $\epsilon = D_g/v$ with quench rate. The physical interpretation of ϕ_f according to Hui et al.[7,8] indicates that it should hardly change with quench rate. So, the effect must be the result of increases in ϵ with sample quench rate.

Since, $D_g \sim \exp(-E_D/RT)$ and $\eta_0 \sim \exp(E_\eta/RT)$, then

$$\epsilon = \frac{D_g}{v} \sim (D_g\eta_0)^{1/2} \sim \left[\exp\left(\frac{E_\eta - E_D}{RT}\right)\right]^{1/2} \qquad (19)$$

where the relation $v \sim (D_g/\eta_0)^{1/2}$ has been used. At constant temperature, ϵ would increase if $E_\eta - E_D$ increases with increasing quench rate. Indeed, the effective activation energies predicted from free-volume theory do depend strongly on the sample's quench history; however, $(E_\eta - E_D)$ is predicted to *decrease* with increasing quench rate (Table 2), which contradicts the expected behavior. It is not clear at this point how to properly account for the effect of quenching on the front reflectivity in the context of the current theory for Case II.

Summary and Conclusion

We found laser interferometry very effective and convenient in studying Case II diffusion in the PMMA/MeOH system. We developed a simple mathematical model which enables calculation of the intensity of light reflected from various layers in a partially swollen polymer film. The model predicts superimposed sinusoids with two dominant frequencies, one of low frequency and high amplitude and another of high frequency and low amplitude. The experiments verified the predictions. An FFT algorithm made it possible to compare actual spectra with modeled spectra to extract three key parameters: The volume fraction of methanol in the swollen layer behind the Case II front, ϕ_e, the Case II front velocity, v, and front reflectivity, rf_2. The temperature-dependent ϕ_e extracted from the data were consistent with the Flory–Huggins theory. Free-volume theory nicely described the temperature dependence of v in annealed samples and made it possible to calculate the individual apparent activation energies for MeOH diffusion in, and viscous flow of, the dry glass. The low values of rf_2 relative to the Fresnel values proves that the Case II front has a finite width on the order of 100 nm. The appearance of a maxima in $|rf_2|$ with temperature in annealed samples could not be explained with Hui et al.'s version of Thomas and Windle's theory[7,8] for the Case II front characteristics (eq 1). On this point, we recommend further experiment and a re-examination of the basic theory.

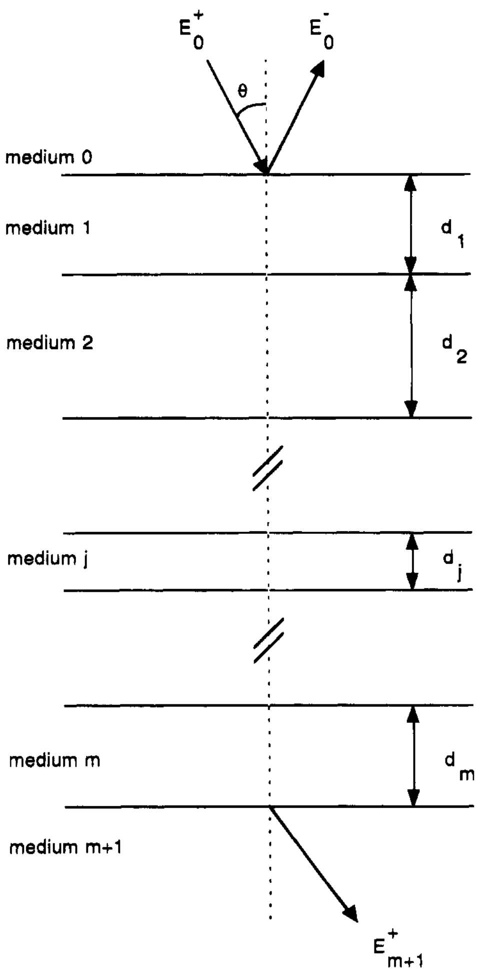

Figure 23. Schematic of a general, multilayered system.

The polymer film's thermal history had a dramatic effect on both v and rf_2. We found with increased quench rate of the samples that v increased significantly, while the apparent activation energies for v decreased. The free-volume theory described these sample thermal history effects fairly well. A decrease in the Case II front's reflectivity with increased cooling rate of the samples was seen, which cannot be reconciled with Hui's version of Thomas and Windle's theory.[7,8] Again, further experiment and a re-examination of the basic theory for Case II is needed to clarify this point.

Acknowledgment. C.J.D. and M.M.H. thank the National Science Foundation (Grant CTS-89-19665) and IBM for financial support. Discussions with Dr. K. Saenger (IBM, Yorktown Heights) and laboratory assistance from Mr. I. Dwan (Columbia University) are acknowledged.

Appendix A

Figure 23 shows the general structure of interest, consisting of a series of layers 1 through m, each homogeneous and transparent. The refractive index of layer i is n_i and its depth is d_i. The interfaces between layers are sharp discontinuities. The stack is bounded on the top and the bottom by semi-infinite media with refractive indices n_0 and n_{m+1}, respectively. The light impinges on the film at an incident angle θ_0. At each interface, a portion of the downgoing wave is transmitted and a portion is reflected. The resultant intensity of all reflections is measured at the detector. The intensity depends on the optical path length differences among the reflections from each interface; i.e., it depends on the extent of constructive or destructive interference.

One can use a matrix method to calculate the reflected intensity from a multilayered structure. In general, the results depend on the polarization of the light but become independent of polarization as $\theta_0 \rightarrow 0$. As our experiments were carried at near-normal incidence, we consider only this limit in what follows.

Denoting the resultant amplitude of the downgoing wave in media j as E_j^+ and that the upgoing wave as E_j^-, Heavens[35] derived

$$\begin{bmatrix} E_{j-1}^+ \\ E_{j-1}^- \end{bmatrix} = \frac{1}{t_j}\begin{bmatrix} e^{i\delta_{j-1}} & r_j e^{i\delta_{j-1}} \\ r_j e^{-i\delta_{j-1}} & e^{-i\delta_{j-1}} \end{bmatrix}\begin{bmatrix} E_j^+ \\ E_j^- \end{bmatrix} \tag{20}$$

for interface j. Here, r_j and t_j are the Fresnel coefficients for reflection and transmission, respectively. The factors $\delta_j = 2\pi n_j(d_j/\lambda)$, with λ being the wavelength of light, give the change in phase for the downgoing wave in traversing the layer j.

Equation 20 enables calculation of the reflected intensity for an arbitrary stack of thin layers. Letting $\mathbf{M}_j$ mean the matrix on the right in eq 20, one finds

$$\mathbf{E}_0 = \prod_{j=1}^{m+1} \mathbf{M}_j \cdot \mathbf{E}_{m+1} \equiv \mathbf{MT} \cdot \mathbf{E}_{m+1} \tag{21}$$

where

$$\mathbf{E}_0 \equiv \begin{bmatrix} E_0^+ \\ E_0^- \end{bmatrix}; \qquad \mathbf{E}_{m+1} \equiv \begin{bmatrix} E_{m+1}^+ \\ 0 \end{bmatrix}$$

The impinging and reflected amplitudes at the top interface are, therefore, related by

$$E_0^- = \frac{MT_{2,1}}{MT_{1,1}} E_0^+ \equiv r_T E_0^+ \tag{22}$$

so that the normalized reflected intensity, R_T, is

$$R_T = r_T r_T^* \tag{23}$$

where the asterisk means the complex conjugate.

Equations 21–23 provide a basis for an approximate calculation of the reflected intensity from any continuous transition layer between two homogeneous, semi-infinite media with different refractive indices since the refractive index profile in such a layer can be approximated by a stack of thin films with systematic variation in the n_j.

Appendix B

Reflected Intensity from the Case II Front, R_{Tf}. The concentration front during Case II transport is not a perfect discontinuity, rather, it is approximately a step-exponential profile when viewed in polymer material coordinates (eqs 1–3; Figure 2). To judge the effects of the characteristic concentrations C_e and C_f and the length scale $\epsilon \equiv D_g/v$ on light reflection from the front, model calculations of the normalized reflected intensity from the front, R_{Tf}, were made for the system poly(methyl methacrylate) (PMMA)/liquid methanol (MeOH) by the matrix procedure described in Appendix A.

Strictly speaking, a conversion to laboratory coordinates is needed. However, for all realistic values of the liquid volume fractions ahead of the front in the PMMA/MeOH system, the deviation between laboratory and material coordinates is at most ~20% in this region. Therefore, we ignored the distinction and assumed a decaying exponential shape of the liquid volume fraction, ϕ, ahead of the front in laboratory coordinates, x (see Figure 2).

The calculation of R_{Tf} with eqs 21–23 in Appendix A was accomplished by assigning the origin (interface 1) to the step discontinuity in the profile and dividing the exponential precursor into 25 equally spaced intervals beginning at the discontinuity and ending where the methanol volume fraction falls to $0.01\phi_f$, with ϕ_f being the volume fraction of methanol corresponding to C_f (see Figure 2). The refractive index in each interval was calculated from its average methanol volume fraction as the volume fraction weighted average of the pure component refractive indices;[38] these were taken as $n_{PMMA} = 1.489$ and $n_{MeoH} = 1.328$.

The effect on R_{Tf} of ϵ and ϕ_f was determined for $\phi_e = 0.2$, which corresponds to an experimental temperature of about 25 °C (see ref 4). The reflected intensity falls sharply with ϵ from the value with $\epsilon = 0$ for a discontinuity in ϕ from ϕ_e to 0, $[(n_e - n_{PMMA})/(n_e + n_{PMMA})]^2$, to the value for a discontinuity from ϕ_e to ϕ_f, $[(n_e - n_f)/(n_e + n_f)]^2$, when $\epsilon \geq 0.2\lambda$. Here n_e and n_f are the refractive indices corresponding to ϕ_e and ϕ_f, respectively. The calculations show clearly that the precursor portion of the front becomes ineffective in reflecting incident light when its characteristic depth exceeds approximately 0.2λ. Consequently, a broad precursor ($\epsilon > 0.2\lambda$) of large amplitude ($\phi_f \simeq \phi_e$) renders the front completely ineffective in reflecting light (i.e, $R_{Tf} \rightarrow 0$).

Reflected Intensity during Case II, $R_T(t)$. We also simulated the steady-periodic signal during Case II to show qualitatively how the signal is affected by the volume fraction of the liquid in the swollen portion, ϕ_e, the moving boundary velocity, v, and the details of the precursor at the front.

The reflected intensity, normalized by the incident intensity, R_T, is given by eq 23 in Appendix A where

$$\mathbf{MT} = \mathbf{M}_1 \cdot \mathbf{MF}_2 \cdot \mathbf{M}_3 \tag{24}$$

Here, the indexing from Figure 3 has been adopted. $\mathbf{M}_1$ characterizes the interface between the fluid and the swollen polymer (interface 1). It contains the Fresnel coefficients based on n_{MeOH} and n_e, where n_e is the refractive index of the swollen polymer having liquid fraction, ϕ_e. The matrix $\mathbf{MF}_2$ characterizes the Case II front (interface 2); it is precisely the product of matrices used in the previous section to calculate R_{Tf} except that the first matrix in the product is replaced by one with the phase factor $\delta_1 = 2\pi n_e(d_1/\lambda)$, where d_1 is the depth of the swollen layer. $\mathbf{M}_3$, characterizing the third interface between dry polymer and substrate, contains the Fresnel coefficient based on n_{PMMA} and the refractive index of the substrate, n_s. $\mathbf{M}_3$ contains a phase factor based on d_2, the depth of the dry, glassy layer.

To simulate the steady-periodic signal during Case II, the time history of R_T was calculated with

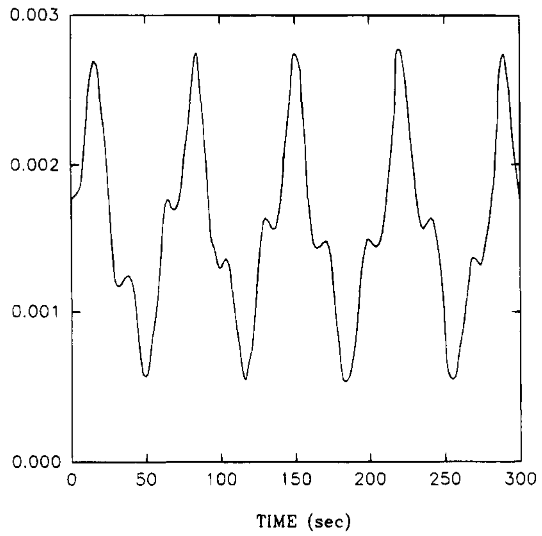

Figure 24. Real-time behavior of R_T according to eqs 21–23. $\phi_e = \phi_f = 0.35$, $\epsilon/\lambda = 0.25$, $l/\lambda = 3.0$, $v/\lambda = 0.01$ Hz.

$$d_1 \simeq \frac{1}{1 - \phi_e} vt$$

$$d_2 \simeq l - vt \tag{25}$$

where l means the depth of the dry film. The above two equations do not account for the induction time in real systems (see Figure 1a); consequently, one cannot mimic the initial behavior observed. Also the relationship for d_2 does not account for the expansion (i.e., swelling) of the film caused by the exponential precursor. The error because of this should be minor since the total amount of liquid associated with the precursor is small. In the calculations, the time history of R_T is traced in the interval $0 \leq t \leq t_{max}$, where $t_{max} = l/v$ is the time for the front to reach the substrate.

The experimental results of Thomas and Windle[4] were used to estimate a reasonable range of values for the moving boundary velocity, v. Their data give $v/\lambda \cong$ 0.001–0.1 Hz for PMMA/MeOH in the range 20–50 °C, with λ being the wavelength of light from a helium–neon laser (6328 Å). Values of l in the range $1-10\lambda$ were employed since these are representative of the thin films employed in our experiments.

Figure 24 shows R_T for a typical case, corresponding closely to our experiments: $\phi_e = \phi_f = 0.35$, $\epsilon/\lambda = 0.25$, $l/\lambda = 3.0$, and $v/\lambda = 0.01$ Hz. The plot shows an oscillatory signal looking qualitatively like the sum of two sinusoids, one of low frequency with a large amplitude and one of higher frequency with a smaller amplitude. As shown in the text, the lower frequency arises from interference between reflections off interface 1 (liquid/swollen polymer) and interface 3 (dry polymer/substrate). The higher frequency arises from the interference between reflections off interface 1 and the concentration front (interface 2). A third frequency is expected from the interference off the front and the glassy polymer/substrate interface, but the amplitude of this contribution is very small. For thicker films (larger l/λ), more low-frequency fringes are seen during the time for the front to traverse the film. A subharmonic "beating" frequency can appear for very thick films ($l/\lambda \geq 10$), manifest as a sinusoidal amplitude envelope.

More interesting are the effects of changing the characteristics of the concentration front. For the system in Figure 24, an increase in ϵ beyond 0.2λ renders the front ineffective in reflecting impinging light and largely removes the contribution of the higher frequency to the signal, leaving only high frequency "shoulders" on the low-frequency fringes.

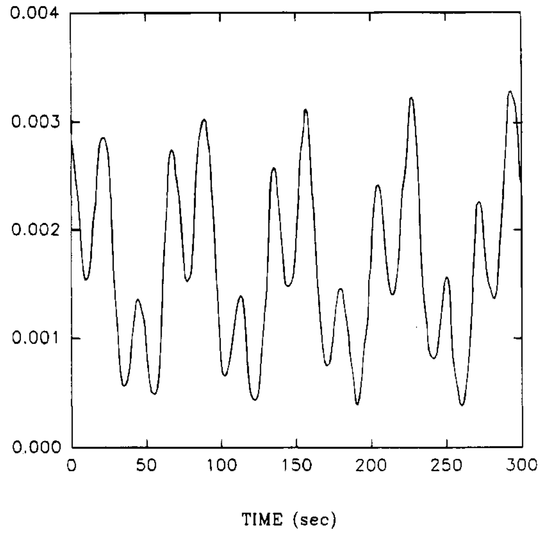

Figure 25. Real-time behavior of R_T according to eqs 21–23. $\phi_e = 0.35$, $\phi_f = 0.175$, $\epsilon/\lambda = 0.25$, $l/\lambda = 3.0$, $v/\lambda = 0.01$ Hz.

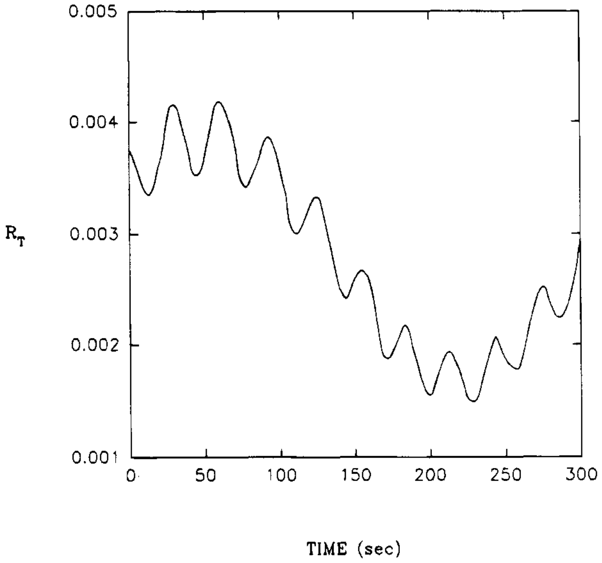

Figure 26. Real-time behavior of R_T according to eqs 21–23. $\phi_e = 0.2$, $\phi_f = 0.1$, $\epsilon/\lambda = 0.25$, $l/\lambda = 3.0$, $v/\lambda = 0.01$ Hz.

Figures 24 and 25 show the effect of reduction in ϕ_f from ϕ_e so that the front approaches a true discontinuity. An increase in amplitude of the high-frequency component results; the minor high-frequency peaks when $\phi_e = \phi_f = 0.35$ and $\epsilon = 0.25\lambda$ (Figure 24) become very prominent as $\phi_f/\phi_e \rightarrow 0$ (Figure 25).

Finally, Figures 25 and 26 show the effects of changes in ϕ_e, the methanol volume fraction in the swollen layer behind the front. A reduction in ϕ_e was made, keeping the ratio $\phi_f/\phi_e = 0.5$. As ϕ_e decays, both dominant frequencies decay, although the lower frequency is reduced by a larger factor. The low frequency is controlled by the speed of the interface 1 relative to interface 3, which falls as ϕ_e decays; the high frequency is controlled by the speed of interface 1 relative to the Case II front which is also affected by ϕ_e but differently, as shown in the text.

References and Notes

(1) Hopfenberg, H. B.; Holley, R. H.; Stannett, V. T. *Polym. Eng. Sci.* **1969**, *9*, 242.
(2) Enscore, D. J.; Hopfenberg, H. B.; Stannett, V.; Berens, A. R. *Polymer* **1977**, *18*, 1105.
(3) Thomas, N.; Windle, A. H. *J. Membr. Sci.* **1978**, *3*, 337.
(4) Thomas, N.; Windle, A. H. *Polymer* **1978**, *19*, 255.
(5) Mills, P. J.; Palmstrom, C. J.; Kramer, E. J. *J. Mater. Sci.* **1986**, *21*, 1479.
(6) Mills, P. J.; Kramer, E. J. *J. Mater. Sci.* **1986**, *21*, 4151.
(7) Hui, C. Y.; Wu, K. C.; Lasky, R. C.; Kramer, E. J. *J. Appl. Phys.* **1987**, *61*, 5129.
(8) Hui, C. Y.; Wu, K. C.; Lasky, R. C.; Kramer, E. J. *J. Appl. Phys.* **1987**, *61*, 5137.
(9) Lasky, R. C.; Kramer, E. J.; Hui, C. Y. *Polymer* **1988**, *29*, 637.
(10) Lasky, R. C.; Kramer, E. J.; Hui, C. Y. *Polymer* **1988**, *29*, 1131.
(11) Fu, T. J.; Durning, C. J. *AIChE J.* **1993**, *39*, 1030.
(12) Vrentas, J. S.; Jarzebski, C. M.; Duda, J. L. *AIChE J.* **1975**, *21*, 894.
(13) Vrentas, J. S.; Duda, J. L. *J. Polym. Sci., Polym. Phys. Ed.* **1977**, *15*, 441.
(14) Peterlin, A. *J. Polym. Sci.* **1965**, *3*, 1083.
(15) Durning, C. J.; Tabor, M. *Macromolecules* **1986**, *19*, 2220.
(16) Thomas, N.; Windle, A. H. *Polymer* **1982**, *23*, 529.
(17) Billovits, G. F.; Durning, C. J. *Chem. Eng. Commun.* **1989**, *82*, 21.
(18) Tong, H. M.; Saenger, K. C.; Durning, C. J. *J. Polym. Sci., Polym. Phys. Ed.* **1989**, *27*, 689.
(19) Ramirez, R. W. *The FFT: Fundamentals and Concepts*; Prentice-Hall: Englewood Cliffs, NJ, 1985.
(20) Thomas, N.; Windle, A. H. *Polymer* **1980**, *21*, 613.
(21) Vrentas, J. S.; Duda, J. L. *Macromolecules* **1976**, *9*, 785.
(22) Vrentas, J. S.; Duda, J. L. *J. Polym. Sci., Polym. Phys. Ed.* **1977**, *15*, 403.
(23) Vrentas, J. S.; Duda, J. L. *J. Polym. Sci., Polym. Phys. Ed.* **1977**, *15*, 417.
(24) Vrentas, J. S.; Duda, J. L. *J. Appl. Polym. Sci.* **1977**, *21*, 1715.
(25) Vrentas, J. S.; Duda, J. L. *J. Appl. Polym. Sci.* **1978**, *22*, 2325.
(26) Vrentas, J. S.; Duda, J. L. *J. Polym. Sci., Polym. Phys. Ed.* **1979**, *17*, 1085.
(27) Vrentas, J. S.; Duda, J. L. *J. Appl. Polym. Sci.* **1980**, *25*, 1793.
(28) Vrentas, J. S.; Duda, J. L. *J. Appl. Polym. Sci.* **1981**, *26*, 3735.
(29) Vrentas, J. S.; Duda, J. L. *AIChE J.* **1982**, *28*, 279.
(30) Ferry, J. D. *Viscoelastic Properties of Polymers*, 3rd ed.; John Wiley & Sons, Inc.: New York, 1980.
(31) Windle, A. H. *J. Membr. Sci.* **1984**, *18*, 87.
(32) Windle, A. H. In *Polymer Permeability*; Comyn, J., Ed.; Elsevier Scientific Publishing Co.: New York, 1985.
(33) Hutchinson, J. M.; Kovacs, A. J. In *The Structure of Non-Crystalline Materials*; Gaskell, Ed.; Taylor & Francis, 1976; p 167.
(34) Struik, L. C. E. *Physical Aging in Amorphous Polymers and Other Materials*; Elsevier Scientific Publishing Co.: New York, 1978.
(35) Heavens, O. S. *Optical Properties of Thin Solid Films*; Dover: New York, 1965.
(36) Glasstone, S. *Textbook of Physical Chemistry*, 2nd ed.; D. Van Nostrand Co. Inc.: New York, 1959.
(37) A referee suggested that the maximum in $|rf_2|$ might be the result of spurious scattering from concentration fluctuations, enhanced as the temperature approaches the Θ temperature from below. Recall that, according to Figure 10, $\Theta \simeq 90$ °C in this system.
(38) This simple relationship gives within ±0.25% the value obtained from a more complex equation by Lorentz and Lorenz,[36] with the assumption of no volume change on mixing.

MA946199F